

Zero-Shot Learning for the Primitives of 3D Affordance in General Objects

Hyeonwoo Kim^{1*} Sookwan Han^{1*} Patrick Kwon² Hanbyul Joo¹

¹Seoul National University ²Naver Webtoon AI

<https://sshowbiz.github.io/ZSP3A/>



Figure 1. Given any 3D object, our method can generate 3D affordance examples involving human-object interactions. By aggregating this dataset into our novel representation, we obtain a unified knowledge of affordance that can be transformed into diverse affordance cues, such as contact, orientation tendency, and spatial relations.

Abstract

One of the major challenges in AI is teaching machines to precisely respond and utilize environmental functionalities, thereby achieving the affordance awareness that humans possess. Despite its importance, the field has been lagging in terms of learning, especially in 3D, as annotating affordance accompanies a laborious process due to the numerous variations of human-object interaction. The low availability of affordance data limits the learning in terms of generalization for object categories, and also simplifies the representation of affordance, capturing only a fraction of the entire affordance. To overcome these challenges, we propose a novel, self-supervised method to “generate” the 3D affordance examples given only a 3D object input, without any manual annotating procedures. The method starts by capturing the 3D object into images and creating 2D affordance examples by inserting humans into the image via inpainting diffusion models, where we present the Adaptive Mask algorithm to enable human insertion without altering the original details of the object. The method consequently lifts inserted humans back to 3D to create 3D human-object pairs, where the depth ambiguity is resolved within a depth optimization framework that utilizes pre-generated human postures from multiple viewpoints. We also provide a novel affordance representation defined on relative orientations and proximity between dense human and object points, that can be easily aggregated from any 3D HOI datasets. The proposed rep-

resentation serves as a primitive that can be manifested to conventional affordance representations via simple transformations, ranging from physically exerted affordances (e.g., contact) to nonphysical ones (e.g., orientation tendency, spatial relations). We demonstrate the efficacy of our method and representation by generating the 3D affordance samples and deriving high-quality affordance examples from the representation, including contact, orientation, and spatial occupancies.

1. Introduction

The unique ability of humans is to perceive the functionalities provided by the environment and to efficiently utilize them; a concept known as affordance [21]. For example, we know what functions a cup provides, set goals responsively during interactions, and precisely control our hands to pick up and use the cup. Such ability allows us to use complex tools in various ways, serving as a major driving factor for our evolution of intelligence. As it is a crucial component of human intelligence, there have been many tries to implement such features in AI and robotics.

Previous studies [11, 16, 24, 25, 30, 35, 89, 92, 94, 96, 107] focus on learning human and object interaction from 2D or 3D dataset in a supervised manner. While these methods provide opportunities to effectively mimic the interactions between humans and environments, such supervised approaches often suffer from a lack of ability to support unseen categories, consequently failing to be generalized to the real world’s diverse interactions. Additionally, the need for labo-

*Equal contribution

rious annotations or data collection procedures makes it hard to scale, limiting the representation of affordance to simple aspects such as expressing affordance categories [6, 32, 47] (e.g., sitting, grasping) or contact heatmap [1, 49] which is just a part of affordance. Thus, the current representation does not completely capture the implicit effects of affordance on the distribution of the agent’s response, such as the orientation tendency of body parts (e.g., face), proximity relations, etc., induced to require various criteria (e.g., physical stability).

Henceforth, we propose a novel method to extract affordance in a zero-shot manner without requiring any manual annotations. Specifically, we address the task of inferring affordance distributions from *any* 3D objects given as mesh; with its first step generating the samples of interacting 3D human and object pairs. We enable this by presenting a novel method, leveraging inpainting diffusion models [75] to insert affordance-aware humans into the renderings of the 3D asset (Sec. 3.2). By creating affordance examples in the relatively “unchallenging” domain of 2D, we can generate plausible samples of affordance without heavy 3D supervision; even with no additional training in 2D as we use pretrained models. However, the challenge exists as directly leveraging the inpainting diffusion model will result in altering the original object, which means the generated affordance is simply a hallucination from a different object. To mitigate this, we propose *Adaptive Mask Inpainting* to preserve the details of the original object and insert humans interacting with the exact target object, rather than hallucinating different ones. We then uplift the predicted humans in 2D back to the 3D space (Sec. 3.3) to generate the 3D affordance samples from 2D images with human pose and shape regressor, where we aim to use for learning 3D affordance. On its path, we also offer a framework that leverages generated 2D affordance samples as depth cues to resolve the inherent depth ambiguity.

Importantly, we also propose a novel affordance representation (Sec. 4) designed to model the prevalent and plausible 3D spatial relationship between a human and an object during interactions. Different from the prior approaches that primarily focus on the 3D contact regions where direct interactions occur [28, 89, 96], our affordance representation encompasses the entire spectrum of relationships between all human parts and object regions, not only the physical contact. Our representation is based on the observation that each part of the human body has a specific set of possible actions in interacting with each part of objects. For example, when we use a laptop, such actions entail not only finger-to-keyboard touch but also involve typical 3D postures, and relative distances of various body parts, including the face and arms. Specifically, our representation encapsulates the relative proximity and orientations between each possible pair of object surface points and human points from generated 3D affordance samples as a probability distribution.

To summarize, our method contributes novel strategies to generate the 3D affordance samples from the given input 3D object, including: (1) adaptive mask inpainting for inserting humans into scenes without harming the original context of the object, and (2) a framework for resolving depth ambiguity of 3D human by leveraging depth cue from synthesized human postures of various viewpoints. Also, we present a (3) novel primitive representation for 3D affordance that captures the full spectrum of relationships among all pairs of human and object points, where we demonstrate efficacy by deriving contact, orientation tendency, and spatial relations.

2. Related Work

Data Synthesis for Learning. There have been approaches to supplement data in fields lacking efficient annotation progress by leveraging generative models, irrespective of the research area. Many methods employ GANs [22, 42] or diffusion models [34, 75, 83] to augment data [31, 88] for various vision tasks, including perception and representation learning [91], classification [9, 56, 87], segmentation [58, 90, 104], dense visual alignment [70], and further extending to 3D tasks, such as neural rendering [27, 102], shape reconstruction [68], and so forth. The major challenge in leveraging synthesized data (or generative models for cues) is controllability, as the generator, even when conditioned, typically produces “free” samples. Ali *et al.* [38] presents a method to control the viewpoint of the synthesized image by modeling the viewpoint-free latent space. CHORUS [26] applies cascaded filtering to the generated dataset to learn 3D human-object spatial relations, similar to our approach.

Learning Visual Affordance. Affordance was introduced by Gibson [21] as a set of functionalities which environment furnishes to an agent (e.g., human, animal). The concept extends to the vision and robotics area, where the focus is on teaching embodied agents to interact with scenes [1, 19, 48, 64, 93], mimicking human-object [2, 8, 13, 17, 29, 36, 41, 50, 62, 71, 73, 77, 84, 100, 101], or hand-object [3–5, 86, 105] interactions. Earlier methods focused on learning action category labels [6, 32, 47] with bounding boxes but lack a full description of affordance. Some studies represent affordance with contact regions and heatmaps on objects [1, 49, 96] or humans [29, 89, 103]. Other than the challenges in representation, annotating affordance, especially in 3D, is challenging due to numerous variations. Previous approaches provide 3D annotations via multi-camera system [2, 37], motion capture [28], and manual process [14, 39, 89, 96]; however, they are limited in terms of categories, thus the model lacks generalization after training. Other approaches train generative models to create affordance samples in 2D [46, 97] or 3D human action [94].

Diffusion Model for Synthesizing Affordance Images. While diffusion models [34, 82, 83] excel at generating realistic images [15, 75], few address the generation of affor-

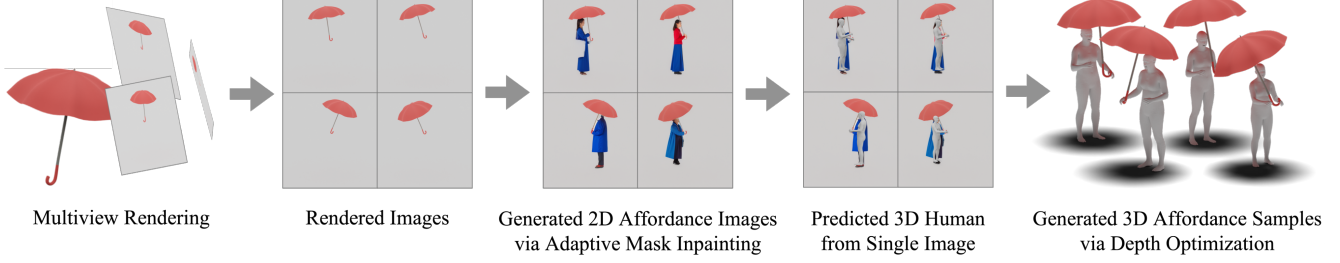


Figure 2. **3D Affordance Sample Generation Method Overview.** The 3D affordane sample generation phase begins by rendering the given 3D object from multiple views. The method leverages inpainting diffusion models to insert humans into rendered object images, creating 2D samples depicting affordance. The method applies Adaptive Mask Inpainting to enable human insertion without harming original details of the object. The method then lifts the 2D humans into 3D through single view 3D human prediction and depth optimization using human cues extracted from generated 2D affordance samples which originally rendered in various views.

dance images (i.e., inserting humans into images). Inpainting models [54, 75], while a common choice for human insertion, often compromise scene details, resulting in inconsistent affordance images. Image editing techniques [33, 59, 61] may offer an alternative but tend to prioritize style and struggle with creating new geometry. Affordance diffusion [97] requires an additional layout network to specify the inpainting region before inserting a hand into the image, and affordance insertion [46] relies on a diffusion model using human images and masks as input, requiring additional training and limiting applicability.

3. 3D Affordance Sample Generation

3.1. Overview

The goal of our method is to infer the affordance distributions $\mathcal{P} = \{\mathcal{P}_{ij}\}$ (defined in Sec. 4) for 3D object meshes from general sources (e.g., Internet) or text-to-3d models [12, 51, 72], without additional annotations. To this end, we “generate” the 3D affordance samples, and consequently use them for affordance distribution learning.

Given an input object mesh $\mathbf{M}_{\text{input}}^o$, our 3D affordance sample generation phase aims to create diverse pairs of 3D humans and objects depicting the type of affordance:

$$\mathcal{D} = \{\mathbf{M}_d^o, \mathbf{M}_d^h\}_{d=1}^D. \quad (1)$$

A d -th object sample \mathbf{M}_d^o is assumed rigid and parametrized as $\{\mathbf{M}_{\text{input}}^o, \mathbf{R}_d^o, \mathbf{t}_d^o\}$ where $\mathbf{t}_d^o \in \mathbb{R}^3$ is the translation and $\mathbf{R}_d^o \in \text{SO}(3)$ is the rotation applied to the input mesh $\mathbf{M}_{\text{input}}^o$. The paired d -th human is parametrized as $\mathbf{M}_d^h = \{\theta_d, \beta_d, \mathbf{R}_d^h, \mathbf{t}_d^h, \mathbf{s}_d^h\}$, where $\theta_d \in \mathbb{R}^{54 \times 3}$ and $\beta_d \in \mathbb{R}^{10}$ are the pose and shape parameters of SMPL-X [69], $\mathbf{t}_d^h \in \mathbb{R}^3$ is translation, $\mathbf{R}_d^h \in \text{SO}(3)$ is the global rotation, and $\mathbf{s}_d^h \in \mathbb{R}$ is scale. Note that we use explicit mesh representation to preserve the surface point orderings $\{\mathbf{v}_i^o\}_{i=1}^{N_o}$, $\{\mathbf{v}_j^h\}_{j=1}^{N_h}$ (used in Sec. 4), where our affordance distribution is learned.

Our 3D affordance sample generation process can be divided into two steps: (1) 2D affordance image generation,

and (2) 2D-to-3D uplifting. The core idea for the first step is to leverage vision-language models [67] and inpainting diffusion models [75] on 2D renderings of input mesh $\mathbf{M}_{\text{input}}^o$ to create diverse examples of 2D affordance from multiple viewpoints. To effectively insert humans into object renderings without altering the original details of the appearance, we present *Adaptive Mask Inpainting*, a method that can be applied to any inpainting diffusion models. In a nutshell, the method specifies the inpainting region over diffusion timesteps, enforcing the model to focus on generating within the *adapted* mask region and preserving the details outside.

The second step, *2D-to-3D uplifting*, focuses on generating 3D samples from the 2D images of humans and objects. Specifically, we first predict the 3D humans from single view images using off-the-shelf [63] 3D human prediction models. To resolve the remaining depth ambiguity of 3D human, we present a novel framework that enables figuring out depth using human cues obtained from generated 2D affordance samples. Refer to Fig. 2 for the overview, and Supp. Mat. for additional details.

3.2. Affordance Image Generation

Rendering Object from Multi-Viewpoints. Given a 3D object $\mathbf{M}_{\text{input}}^o$, we first render it from multiple viewpoints. We place the object and camera differently for two object types: *static* and *dynamic*. For objects that are presumed to be fixed on the ground during interaction (e.g., chair), we fix the object on the ground plane, whereas objects with dynamic pose during interaction (e.g., cup) are perturbed with sampled rotation and translation. We empirically find that differentiating the rendering process per object type improves inpainting quality when using diffusion models as they inherently possess spatial bias for a given object. Note that we automate this process by rendering the object at any direction first and inferring the object type via vision-language model [67]. For rendering, we use weak perspective cameras $\{\Pi_c\}_{c=1}^N$ installed around the object with equal interval azimuth and same elevation, where N is set as 8 for *static*, 40 for *dynamic* objects.

Algorithm 1 Adaptive Mask Inpainting

Latent Diffusion Model: ϵ_θ
Latent VAE Decoder: \mathbf{D}
Segmentation Model: \mathbf{S}
DDIMSchedule: $\{\alpha_t\}_{t=1}^T$
Inputs: Prompt (c), Initial Mask (m_{default}), Image (I_{orig})
Initialize Noise Latent: $x_T \sim \mathcal{N}(\mathbf{0}, \mathbf{I})$
Initialize Adaptive Mask: $m_T \leftarrow m_{\text{default}}$
for $t=T, \dots, 1$ **do**
 $\hat{x}_0 = \frac{1}{\sqrt{\alpha_t}}(x_t - \sqrt{1 - \alpha_t}\epsilon_\theta(x_t; c, m_t, I_{\text{orig}}, t))$
 if $t \in \text{ProvokeSchedule}$ **then**
 $s = \mathbf{S}(\mathbf{D}(\hat{x}_0))$
 if $s \neq \emptyset$ **then**
 $m_{t-1} = \text{Dilate}(s)$
 else
 $m_{t-1} = m_{\text{default}}$
 end if
 else
 $m_{t-1} = m_t$
 end if
 $x_{t-1} = \text{DDIMStep}(x_t, \hat{x}_0, t)$
end for
return $\mathbf{D}(x_0)$

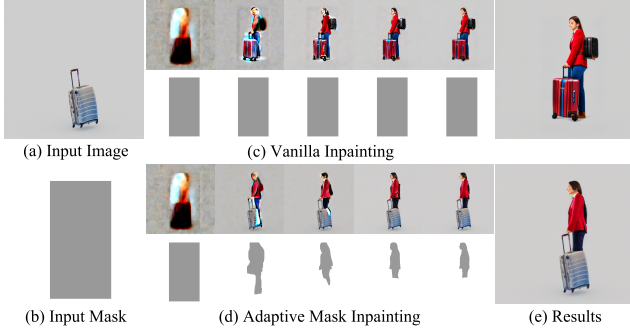


Figure 3. **Adaptive Mask Inpainting.** Without adaptive mask inpainting, the original object is damaged when inserting humans.

Inpainting Mask Selection. After rendering the images, we select the masks on which we inpaint a human interacting with the object. We move a sliding window and select the windows if the intersection over the object segmentation mask satisfies a certain threshold.

Prompt Generation. Inspired by CHORUS [26], we automatically generate the prompts that describe the possible interactions with humans and the given object, which are taken as guidance for inpainting. Specifically, we utilize the vision-language model [67] to infer the HOI prompt using the rendered object image and predefined template. We generate 3 prompts per given object. See Supp. Mat. for additional details.

Adaptive Mask Inpainting for Human Insertion. We synthesize 2D images of human-object interaction by inpainting

the human into rendered object images using publicly available text-conditional inpainting diffusion models [75]. However, the challenge arises as the object geometry and details within the mask region are not preserved during inpainting, raising the odds of creating hallucinations of affordance. To mitigate this problem, we present *Adaptive Mask Inpainting* to progressively specify the inpainting region over diffusion timesteps. Let the sequence of denoised image latent be $\{x_t\}_{t=T}^0$, where x_T is the fully random noise and x_0 is the denoised latent. Inspired by the observation that the quality of the predicted denoised image \hat{x}_0 improves over progress of timestep, and creates a low-level structure of the target prompt (in this case, human) even at the early steps as shown in Fig. 3, we aim to *adapt* the inpainting region m_t over timesteps by spatially discovering the mask from the low-level structure. Specifically, we apply PointRend [44] to decoded latent $\mathbf{D}(\hat{x}_0)$ at specific timesteps to predict the human mask, consequently use as the mask for the next denoising step. We find our approach better preserves the target objects as demonstrated in our experiments. Note that we dilate the predicted human mask to tolerate the imperfection of the generated structure during early steps. Refer to Algorithm. 1 for the full pipeline.

3.3. Lifting 2D Affordance to 3D

From the previous section, we obtain a set of affordance images $\{I_d\}_{d=1}^D$. Even though we have multiple views with geometrically consistent object renderings, the inserted humans have diversity without multi-view consistency, and thus it is non-trivial to directly lift 3D humans from these 2D images. To address this, we first utilize a single view 3D human prediction model to obtain a corresponding 3D human pose and shape of the image, and then estimate the depth of the human with weak auxiliary cue provided by the set of affordance images, generating a 3D affordance sample corresponds to the image.

Single View 3D Human Prediction. To uplift the 2D affordance images into 3D, we first predict the pose and shape of 3D humans from the images. We apply off-the-shelf 3D human prediction model [63] (denoted as $\mathbf{F}_{\text{human}}$) to predict SMPL-X humans [69] from generated images:

$$\{\theta_d, \beta_d, \mathbf{j}_d, \mathbf{R}_d^h, \mathbf{s}_d^h, x_d, y_d\} = \mathbf{F}_{\text{human}}(I_d) \quad (2)$$

, where $\theta_d \in \mathbb{R}^{54 \times 3}$, $\beta_d \in \mathbb{R}^{10}$, $\mathbf{j}_d \in \mathbb{R}^{67 \times 3}$ are the predicted SMPL-X pose, shape, and joints (see Supp. Mat. for the increased number of joints), respectively. Note that \mathbf{j}_d is defined in world coordinate shared with weak perspective cameras, obtained by transforming joints with camera rotation and translation. $\mathbf{R}_d^h \in \text{SO}(3)$ is global rotation, and the \mathbf{s}_d^h, x_d, y_d are scale, and x, y direction offsets representing the parameters of weak-perspective camera Π_d assigned to image I_d . As 3D human lies within the weak perspective camera framework, there remains depth ambiguity to solve.

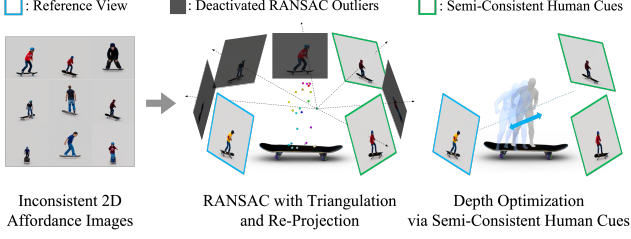


Figure 4. **Leveraging Inpainted Images for Specifying Depth.** From inconsistent 2D affordance images, we apply RANSAC [18] to figure out largest inlier set which is semi-consistent with reference view image. The inlier set are used to resolve depth ambiguity.

Depth Optimization using Weak Auxiliary Cue To address the depth ambiguity of 3D human obtained from reference image, we leverage 2D affordance images generated in advance. Since the human pose in images are geometrically inconsistent, we select the largest subset inliers \mathcal{I} among them which are “semi-consistent” with the reference image by applying RANSAC [18] in terms of joint re-projection error. The joint triangulation is performed on two images, including the reference image. Note that we generate sufficiently large amount of 2D affordance images to ensure the existence of the inlier set. The inliers \mathcal{I} is used for specifying depth z_d , as shown in Fig. 4 via depth optimization by minimizing the joint re-projection loss defined below:

$$\mathcal{L}_{\text{re-projection}} = \frac{1}{|\mathcal{I}|} \sum_{I_{d'} \in \mathcal{I}} \|\Pi_{d'}(\mathbf{j}_d + z_d \mathbf{f}_d) - \Pi_{d'}(\mathbf{j}_{d'})\|^2 \quad (3)$$

where $\Pi_{d'}$, $\mathbf{j}_{d'}$ denotes the weak perspective projection and predicted 3D joints in world coordinate w.r.t. the inlier image $I_{d'}$, and $\mathbf{f}_d \in \mathbb{R}^3$ is the normalized direction of the camera Π_d . For initial depth before optimization, we leverage occlusion cues which human segmentation provides as a depth ordering between human and object, inspired by Jiang *et al.* [40]. Around the object location, we initialize equispaced 7 SMPL-X along the camera direction and select the one with the best IoU between the rendered mask (regarding occlusion) and segmentation from the image. The initialization is helpful in the case when optimal position of object is between two human body parts along the camera direction (e.g., body of motorcycle is placed between human legs while riding), which collision loss (which will be explained next) often prevents human from crossing the object while optimization. See Supp. Mat. for additional details.

We also leverage a collision cue to estimate fine-grained depth, considering physical plausibility. We adopt collision loss from COAP [60] where the human body is represented as SDF [65] field. We set object vertices as query points to reduce the collision between human and object, namely $\mathcal{L}_{\text{collision}}$. We optimize depth z_d to minimize the total loss:

$$\mathcal{L} = \mathcal{L}_{\text{re-projection}} + \lambda_{\text{collision}} \mathcal{L}_{\text{collision}} \quad (4)$$

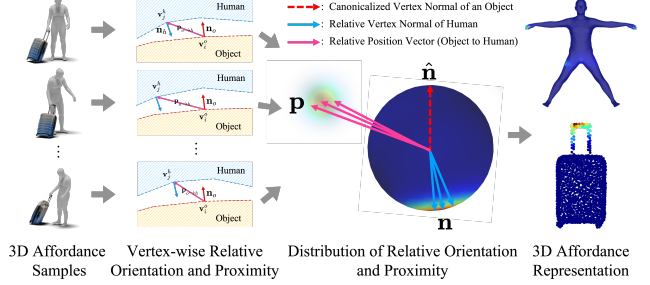


Figure 5. **Visualization of Primitive Representation.** For each human and object point, the primitive is represented as probabilistic distribution of relative normal and proximity after canonicalization.

Filtering. We filter out potentially low-quality 3D human samples in the cases of: (1) human rendering (regarding occlusion) and predicted human segmentation do not overlap much; (2) number of inliers during RANSAC is small; (3) human and object collides significantly in 3D.

4. Primitive Representation of 3D Affordance

Given an ordered 3D surface points of an object, we aim to model the pointwise affordance distributions that encapsulates proximity and orientations of a human surface point from human body (or vice versa, which we omit for brevity). In practice, we use our 3D affordance samples $\mathcal{D} = \{\mathbf{M}_d^o, \mathbf{M}_d^h\}_{d=1}^D$ consists of object mesh \mathbf{M}_d^o and generated 3D human mesh \mathbf{M}_d^h . For each sample in \mathcal{D} , we apply Poisson-disk sampling [57] to uniformly select the points $\{\mathbf{v}_i^o\}_{i=1}^{N_o}$ and $\{\mathbf{v}_j^h\}_{j=1}^{N_h}$ on each surface. The density function on the i -th object vertex \mathbf{v}_i^o and the j -th human vertex \mathbf{v}_j^h , which we denote as $\mathcal{P}_{ij}(\mathbf{p}, \mathbf{n})$, represents the probability (of the occurrence) of the relative position $\mathbf{p} \in \mathbb{R}^3$ and relative normal orientation $\mathbf{n} \in \mathbb{S}^2$ of the human point \mathbf{v}_j^h with respect to object point \mathbf{v}_i^o within the 3D affordance samples. When we compute \mathbf{p} and \mathbf{n} , we canonicalize the orientation of the human surface normal \mathbf{n}_j^h and relative position $\mathbf{p}^{o \rightarrow h} = \mathbf{v}_j^h - \mathbf{v}_i^o$, assuming the object surface normal \mathbf{n}_i^o is rotated to face $\hat{\mathbf{n}} = [0, 0, 1]^T$ as shown in Fig. 5 (details in Supp. Mat.). The \mathcal{P}_{ij} sums up to 1 for all possible \mathbf{p} and \mathbf{n} :

$$\int_{\mathbb{R}^3} \int_{\mathbb{S}^2} \mathcal{P}_{ij}(\mathbf{p}, \mathbf{n}) d\mathbf{n} d\mathbf{p} = 1 \quad (5)$$

In practice, we set the domain of \mathbf{p} as voxelized grid and domain of \mathbf{n} as equispaced grid on \mathbb{S}^2 , obtained via Fibonacci Spirals [20], and compute the discrete probabilities by aggregating Gaussian Kernels calculated for \mathbf{n} and \mathbf{p} (we use geodesic metrics for \mathbf{n}). Under the probability distribution $\mathcal{P}_{ij}(\mathbf{p}, \mathbf{n})$, we define three different types of functions $f(\mathbf{p}, \mathbf{n})$ to capture different aspects of affordances: (1) Contactual affordance, (2) Orientational affordance, (3) Spatial affordance. Given each function $f(\mathbf{p}, \mathbf{n})$ described below, the pointwise affordance of object vertex \mathbf{v}_i^o w.r.t. human

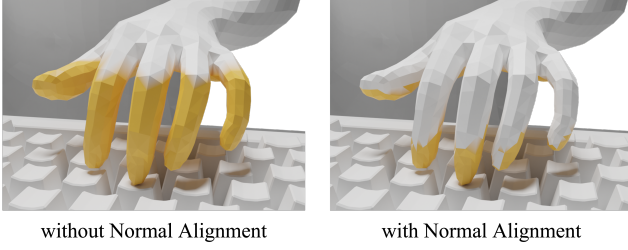


Figure 6. **Effects of Normal Alignment when deriving contact map.** The normal alignment term improves precision when computing contact scores, compared to when only proximity is considered.

vertex \mathbf{v}_j^h is determined by computing its expectation:

$$\mathbb{E}_{\mathbf{p}, \mathbf{n} \sim \mathcal{P}_{ij}} [f(\mathbf{p}, \mathbf{n})] \quad (6)$$

Contactual Affordance. From the learned primitives, we can easily infer the contactness between arbitrary object surface point \mathbf{v}_j^o and human surface point \mathbf{v}_i^h regarding proximity and normal alignment as:

$$f_{\text{contact}}(\mathbf{p}, \mathbf{n}) = \left(\frac{1 - \mathbf{n} \cdot \hat{\mathbf{n}}}{2} \right) e^{-\|\mathbf{p}\|} \quad (7)$$

where the $e^{-\|\mathbf{p}\|}$ term encourages high score when distance $\|\mathbf{p}\|$ is near. The $\frac{1 - \mathbf{n} \cdot \hat{\mathbf{n}}}{2}$ term, motivated by the concept of the normal force that physical interactions are conducted via exerted normal force between contact points, encourages high score when the normals of \mathbf{v}_j^o and \mathbf{v}_i^h align in antiparallel direction. As shown in Fig. 6, the normal alignment term improves the precision of the contact map, especially when small body parts (e.g., fingertips) interact with an object and allows more robust affordance learning even when using noisy HOI datasets, compared to prior work that only introduces proximity for contact terms [2, 28, 29, 98, 103] or normal for computing only penetration [23, 95], without considering the alignment of surface normals.

Oriental Affordance. We aim to capture the pattern and tendency of the orientation of body parts with respect to the object based on the concept of Shannon entropy [79]. Intuitively, low entropy means there exists less uncertainty or more typical patterns of human body orientations during the interactions. To quantify the orientational tendency for affordance representation, we use negated normalized Shannon entropy to enforce high value when the human surface normal shows consistent orientational tendency (low variance) with respect to the object surface normal:

$$f_{\text{orientation}}(\mathbf{n}) = 1 + \frac{\log \mathcal{P}_{ij}(\mathbf{n})}{\log n_b} \quad (8)$$

where n_b denotes the number of discretized bins of probability measure. Intuitively, the Oriental Affordance defined by $\mathbb{E}_{\mathbf{n} \sim \mathcal{P}_{ij}} [f_{\text{orientation}}(\mathbf{n})]$ has a low value when marginalized distribution $\mathcal{P}_{ij}(\mathbf{n})$ is close to the uniform distribution,

meaning that there is no dominant orientational pattern. Note that Eq. 8 is agnostic to the proximity term \mathbf{p} , which allows us to model the nonphysical orientational effects for even far-distance points as shown in Fig. 9.

Spatial Affordance. Following CHORUS [26], we also consider the 3D spatial occupancy distribution of a human surface point with respect to the object points by simply counting the occurrence:

$$f_{\text{spatial}}(\mathbf{p}) = \mathbf{1}(\mathbf{x} - \mathbf{p}) \quad (9)$$

where $\mathbf{1}(\cdot) : \mathbb{R}^3 \rightarrow \{0, 1\}$ is a binary function that returns 1 if the given argument is zero vector else 0, thus the the Spatial Affordance $\mathbb{E}_{\mathbf{p} \sim \mathcal{P}_{ij}} [f_{\text{spatial}}(\mathbf{p})]$ is a function that outputs scalar occupancy for the given spatial vector $\mathbf{x} \in \mathbb{R}^3$. In practice we implement the function as voxel array, counting 1 to the voxel that contains \mathbf{p} . Note that f_{spatial} is agnostic to the normal direction \mathbf{n} via marginalization. Learning the occupancy informs us about macro positioning of the human with respect to the given object, exemplified in Fig. 10.

5. Experiments

In Sec. 5.2, we perform quantitative evaluation to determine the strength of our 3D affordance sample generation pipeline. We validate the effect of depth optimization via weak auxiliary cues by comparing the generated samples with existing 3D HOI dataset [2]. We also compare our Adaptive Mask algorithm with original inpainting baseline to prove the scene-preservability during inpainting. In Sec. 5.3, we qualitatively demonstrate the efficacy of our generated dataset and our new representation by showcasing multiple examples of different affordance types. We illustrate the generalizability of our method by generating high-quality contact maps for various 3D objects from various sources. Additionally, we analyze contact representations on both human and object, aggregated on specific subsets of points, exploring the potential for modeling dense, region-wise contact. Furthermore, we examine the exemplified results of orientational affordance and spatial affordance.

5.1. Datasets

Our method generates the 3D affordance samples in a self-supervised manner. We prepare the input 3D objects from various sources listed below.

3D Object Datasets. We sample the object meshes from various sources, including conventional 3D object datasets and Internet source. For conventional 3D object datasets, we test our method on 3 objects from ShapeNet [10], 5 objects from InterCap [37] and 20 objects from BEHAVE [2]. We generate the texture for InterCap using TEXTure [74] as the dataset does not provide the texture. To test the generalizability of our method, we apply our method on the objects obtained from the Internet source. Specifically, we use 4 objects from SketchFab [81].

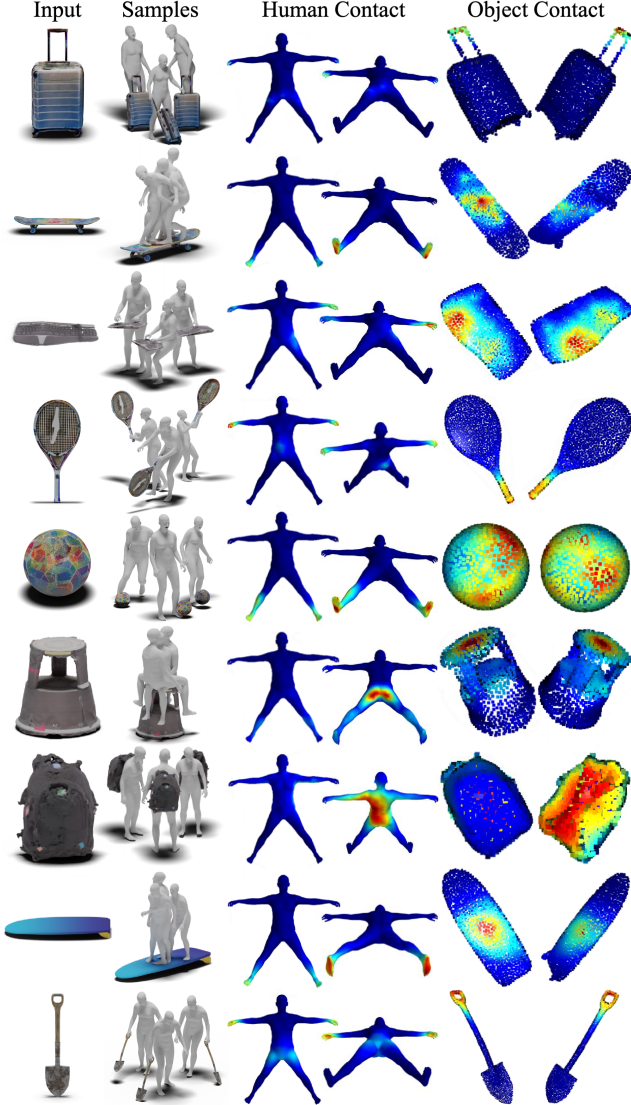


Figure 7. **Contact Results on Various 3D Objects.** Using only the generated 3D affordance samples, our representation can effectively infer precise contact information.

BEHAVE Dataset. For quantitative evaluation, we utilize BEHAVE [2] dataset as ground-truth to verify the quality of generated 3D affordance samples. BEHAVE [2] contains video sequences of HOI scenarios for 20 object categories. Each video frame is annotated with a single 3D human and object, where each 3D human is annotated as SMPL-H [53, 76] parameters and 3D objects as rotation and translation applied to the canonical mesh. We preprocess the dataset by transferring the SMPL-H annotations into SMPL-X format following Choutas *et al.* [69], and downsampling human and object mesh into 1000 surface points described in Sec. 4.

5.2. Quantitative Evaluation

Effects of Adaptive Mask Inpainting. We verify the effectiveness of our adaptive mask algorithm, by comparing

Table 1. **Effects of Adaptive Mask Inpainting.** Adaptive mask inpainting effectively inserts human into scene images without harming the original scene.

Inpainting Methods	RMSE _{Background} ↓	mIoU↑	mIoU _{Occlusion Aware} ↑
Vanilla	36.20	0.64	0.74
Adaptive Mask	17.45	0.73	0.83

Table 2. **Effects of Depth Optimization via Multiview Cues.** Resolving depth ambiguity via selecting semi-consistent multiview cues improves the quality of affordance data in 3D.

Methods	SIM _{Human} ↑	SIM _{Object} ↑
Ours _{w/o} Depth Optimization via Weak Auxiliary Cues	25.77	34.20
Ours _{full}	33.21	46.75

the amount of background preservation for inpainted images with the original inpainting diffusion model. We report 3 metrics; (1) RMSE_{Background}: pixel error between images excluding the predicted human region; (2) mIoU: average IoU between object predictions in each inpainted image and original object image; (3) mIoU_{Occlusion Aware}: same metric as (2) but excluding the predicted human region during computation. To ensure fairness, we predict high-quality human/object segmentation from images using open vocabulary segmentation model [45, 52], different from PointRender [44] used in adaptive mask algorithm. As shown in Tab. 1, we demonstrate our adaptive mask algorithm better preserves the background, not only pixelwise (RMSE_{Background}), but also semantic-region-wise (mIoU, mIoU_{Occlusion Aware}) than original mask inpainting baseline. This means that the generated images from adaptive mask inpainting are more likely to preserve the original object, and not create *hallucinated*, or geometric implausible affordance.

Effects of Depth Optimization via Weak Auxiliary Cues.

We justify our optimization pipeline by comparing the quality of the generated 3D affordance samples produced with and without the component. Specifically, we ablate this component by directly using the depth initialization results obtained from human segmentation cues (refer to Sec. 3.3), without further depth optimization. We extract the primitive representations from the generated dataset (\mathcal{P}_{ij}) and ground-truth primitive representations from BEHAVE [2] dataset ($\mathcal{P}_{ij}^{\text{GT}}$), where we consequently compute similarity [85] between aggregated human contact (i.e., SIM_{Human}) and aggregated object contact (i.e., SIM_{Object}), derived from each \mathcal{P}_{ij} and $\mathcal{P}_{ij}^{\text{GT}}$. Note that we simply select maximum score among i or j for aggregation. The motivation using contact as metric is because it is a widely used affordance cue, and a conventional way to represent 3D affordance knowledge. As shown in Tab. 2, we observe a big performance drop without our depth optimization framework. This is expected, as solely relying on segmentation cues for depth prediction will not provide precise depth, and does not regard the plausibility of human joints observed from different views, causing 3D artifacts such as floating humans.

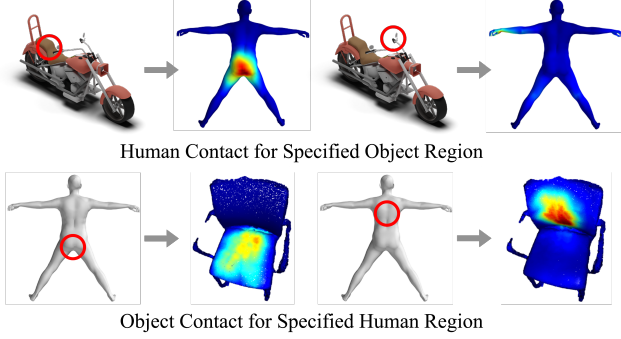


Figure 8. **Contact for Specified Region.** Our representation provides contact scores for all pairs of human point and object point, which can be used to infer regionwise contact map.

5.3. Qualitative Evaluation

Contact Results on Various 3D Objects. We demonstrate the quality of the generated dataset, derived human and object contact map from our representation for various objects in Fig. 7. Note that we show the aggregated contact map, obtained via maximizing score. The results demonstrate the quality of the generated dataset, and preciseness of the contact map derived from our representation.

Contact for Specified Regions. Our representation outputs contact values for each pair of human point and object point; which means we can infer corresponding contact region w.r.t. specified human or object region by simply selecting the points and aggregating the contact values. See the first row of Fig. 8. For the selected points on the handle of the motorcycle, we can observe the human contact possessing high values around hand, while selecting points on the seat of the motorcycle gives high values of human contact around buttocks. This is plausible, as handle provides utilities to steer motorcycle by hand, and seat provides a physical support via buttocks. The second row shows the “inverse” results, where selecting the human surface points around buttocks gives high contact values for object around the seat, while selecting the points around back gives high values around backrest. Enabling learning for such dense contact correspondences for any object opens up a range of possible future work.

Orientalional & Spatial Affordance. Example of orientalional affordance is shown in Fig. 9. As seen in the figure, the orientation tendency shows overall higher score in the case of chair, compared to the stool. This results comes from the geometry of the chair, as the chair with backrest and handles will induce human front torso to head front, as heading back or side will likely cause collision with the object, making the pose highly likely to be physically implausible. In contrast, we observe low scores in the case of stool, as no structure exists above the seating, hence the human becoming freely rotatable w.r.t. azimuth, and deriving low orientation tendency (high entropy). Note that we observe high values on thighs and top of the head as those body parts are implicitly

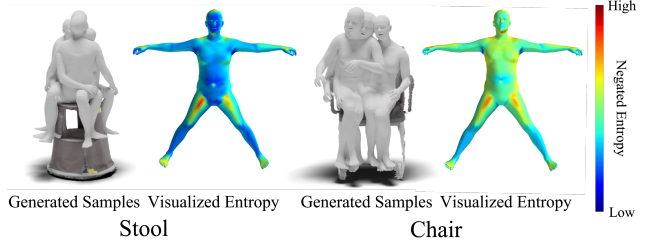


Figure 9. **Orientalional Affordance.** The chair with backrest provides higher orientation tendency (given as negated entropy) for the torso than the stool with arbitrary sitting directions.

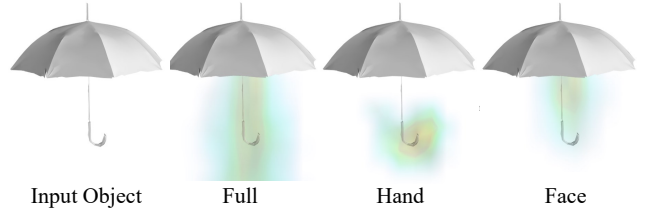


Figure 10. **Spatial Affordance.** By selecting the points from specific body parts of human, we can derive the spatial occupancy distribution for any body parts w.r.t. the object.

headed antiparallel to gravity while sitting. In Fig. 10, we also exemplify the use of spatial affordance, where we show relative human occupancy given the object umbrella. Similar to contact, since we save the vertex-wise occupancy scores, we can specify the human points and check the occupancy of the selected points only (e.g., hands or faces). As shown, we can observe that the hand occupies volume around the handle, and face in the region inside and near the umbrella, which is plausible assuming that human grabs the umbrella, and uses it to block face from the rain by hiding under it.

6. Discussion

We introduce a novel method to learn 3D affordance for any 3D object input, by generating the 3D affordance samples for the specific object, which is a pair of human and object mesh depicting plausible interaction. The method leverages zero-shot capabilities of inpainting diffusion models for generalization, with novel strategies including adaptive mask inpainting to enable scene-preserving human insertion, and depth optimization framework that leverages generated human cues from multiple viewpoints to uplift 2D affordance image into 3D. Furthermore, we propose new primitive affordance representation, where we demonstrate the potential by deriving various types of affordance, including contact, orientation tendency, and spatial occupancy. With our method being generalizable, and our representation being easily extractable, our approach offers myriads of possible applications. Despite the potentials, the method is new and possesses limitations such as challenges in learning dexterous grasps. See Supp. Mat. for further discussion on limitations and potential future work.

Acknowledgements. This work was supported by Naver Webtoon. The work of SNU members was also supported by NRF grant funded by the Korean government (MSIT) (No. 2022R1A2C2092724), and IITP grant funded by the Korean government (MSIT) (No.2021-0-01343). H. Joo is the corresponding author.

References

- [1] S. Bahl, R. Mendonca, L. Chen, U. Jain, and D. Pathak. Affordances from human videos as a versatile representation for robotics. In *CVPR*, 2023. 2
- [2] B. L. Bhatnagar, X. Xie, I. Petrov, C. Sminchisescu, C. Theobalt, and G. Pons-Moll. Behave: Dataset and method for tracking human object interactions. In *CVPR*, 2022. 2, 6, 7, 12, 15
- [3] S. Brahmbhatt, C. Ham, C. C. Kemp, and J. Hays. Contactdb: Analyzing and predicting grasp contact via thermal imaging. In *CVPR*, 2019. 2
- [4] S. Brahmbhatt, A. Handa, J. Hays, and D. Fox. Contactgrasp: Functional multi-finger grasp synthesis from contact. In *IROS*, 2019.
- [5] S. Brahmbhatt, C. Tang, C. D. Twigg, C. C. Kemp, and J. Hays. Contactpose: A dataset of grasps with object contact and hand pose. In *ECCV*, 2020. 2
- [6] M. Cai, K. M. Kitani, and Y. Sato. Understanding hand-object manipulation with grasp types and object attributes. In *RSS*, 2016. 2
- [7] Z. Cao, G. Hidalgo Martinez, T. Simon, S. Wei, and Y. A. Sheikh. Openpose: Realtime multi-person 2d pose estimation using part affinity fields. *IEEE TPAMI*, 2019. 13
- [8] Z. Cao, H. Gao, K. Mangalam, Q.-Z. Cai, M. Vo, and J. Malik. Long-term human motion prediction with scene context. In *ECCV*, 2020. 2
- [9] L. Chai, J.-Y. Zhu, E. Shechtman, P. Isola, and R. Zhang. Ensembling with deep generative views. In *CVPR*, 2021. 2
- [10] A. X. Chang, T. Funkhouser, L. Guibas, P. Hanrahan, Q. Huang, Z. Li, S. Savarese, M. Savva, S. Song, H. Su, J. Xiao, L. Yi, and F. Yu. ShapeNet: An Information-Rich 3D Model Repository. Technical Report arXiv:1512.03012 [cs.GR], 2015. 6, 14
- [11] Y.-W. Chao, W. Yang, Y. Xiang, P. Molchanov, A. Handa, J. Tremblay, Y. S. Narang, K. Van Wyk, U. Iqbal, S. Birchfield, et al. Dexycb: A benchmark for capturing hand grasping of objects. *CVPR*, 2021. 1
- [12] R. Chen, Y. Chen, N. Jiao, and K. Jia. Fantasia3d: Disentangling geometry and appearance for high-quality text-to-3d content creation. 2023. 3
- [13] Y. Chen, S. Huang, T. Yuan, S. Qi, Y. Zhu, and S.-C. Zhu. Holistic++ scene understanding: Single-view 3d holistic scene parsing and human pose estimation with human-object interaction and physical commonsense. In *ICCV*, 2019. 2
- [14] S. Deng, X. Xu, C. Wu, K. Chen, and K. Jia. 3d affordancenet: A benchmark for visual object affordance understanding. In *CVPR*, 2021. 2
- [15] A. R. et al. Hierarchical text-conditional image generation with clip latents. *arXiv preprint arXiv:2204.06125*, 2022. 2
- [16] Z. Fan, O. Taheri, D. Tzionas, M. Kocabas, M. Kaufmann, M. J. Black, and O. Hilliges. Articulated objects in free-form hand interaction. *CVPR*, 2023. 1
- [17] M. Fieraru, M. Zanfir, E. Oneata, A.-I. Popa, V. Olaru, and C. Sminchisescu. Three-dimensional reconstruction of human interactions. In *CVPR*, 2020. 2
- [18] M. A. Fischler and R. C. Bolles. Random sample consensus: a paradigm for model fitting with applications to image analysis and automated cartography. *Communications of the ACM*, 1981. 5, 13
- [19] W. Gao and R. Tedrake. kpm-sc: Generalizable manipulation planning using keypoint affordance and shape completion. In *ICRA*, 2021. 2
- [20] M. Garg, P. Garg, and R. Vohra. Advanced fibonacci sequence with golden ratio. *IJSE*, 2014. 5
- [21] J. J. Gibson. *The Ecological Approach to Visual Perception*. Houghton Mifflin, 1979. 1, 2
- [22] I. Goodfellow, J. Pouget-Abadie, M. Mirza, B. Xu, D. Warde-Farley, S. Ozair, A. Courville, and Y. Bengio. Generative adversarial nets. In *NeurIPS*, 2014. 2
- [23] P. Grady, C. Tang, C. D. Twigg, M. Vo, S. Brahmbhatt, and C. C. Kemp. ContactOpt: Optimizing contact to improve grasps. In *CVPR*, 2021. 6
- [24] S. Hampali, M. Rad, M. Oberweger, and V. Lepetit. Honnotate: A method for 3d annotation of hand and object poses. *CVPR*, 2020. 1
- [25] S. Hampali, S. D. Sarkar, M. Rad, and V. Lepetit. Key-point transformer: Solving joint identification in challenging hands and object interactions for accurate 3d pose estimation. *CVPR*, 2022. 1
- [26] S. Han and H. Joo. Learning canonicalized 3d human-object spatial relations from unbounded synthesized images. In *ICCV*, 2023. 2, 4, 6, 14
- [27] Z. Hao, A. Mallya, S. Belongie, and M.-Y. Liu. Gancraft: Unsupervised 3d neural rendering of minecraft worlds. In *ICCV*, 2021. 2
- [28] M. Hassan, V. Choutas, D. Tzionas, and M. J. Black. Resolving 3d human pose ambiguities with 3d scene constraints. In *ICCV*, 2019. 2, 6
- [29] M. Hassan, P. Ghosh, J. Tesch, D. Tzionas, and M. J. Black. Populating 3d scenes by learning human-scene interaction. In *CVPR*, 2021. 2, 6
- [30] Y. Hasson, G. Varol, D. Tzionas, I. Kalevtykh, M. J. Black, I. Laptev, and C. Schmid. Learning joint reconstruction of hands and manipulated objects. In *CVPR*, 2019. 1
- [31] R. He, S. Sun, X. Yu, C. Xue, W. Zhang, P. Torr, S. Bai, and X. Qi. Is synthetic data from generative models ready for image recognition? *arXiv preprint arXiv:2210.07574*, 2022. 2
- [32] T. Hermans, J. M. Rehg, and A. Bobick. Affordance prediction via learned object attributes. In *Proc. Intl. Conf. on Robotics and Automation*, 2011. 2
- [33] A. Hertz, R. Mokady, J. Tenenbaum, K. Aberman, Y. Pritch, and D. Cohen-Or. Prompt-to-prompt image editing with cross attention control. *arXiv preprint arXiv:2208.01626*, 2022. 3
- [34] J. Ho, A. Jain, and P. Abbeel. Denoising diffusion probabilistic models. *arXiv preprint arxiv:2006.11239*, 2020. 2

- [35] C.-H. P. Huang, H. Yi, M. Höschle, M. Safroshkin, T. Alexiadis, S. Polikovsky, D. Scharstein, and M. J. Black. Capturing and inferring dense full-body human-scene contact. In *CVPR*, 2022. 1
- [36] C.-H. P. Huang, H. Yi, M. Höschle, M. Safroshkin, T. Alexiadis, S. Polikovsky, D. Scharstein, and M. J. Black. Capturing and inferring dense full-body human-scene contact. In *CVPR*, 2022. 2
- [37] Y. Huang, O. Taheri, M. J. Black, and D. Tzionas. InterCap: Joint markerless 3D tracking of humans and objects in interaction. In *GCPR*, 2022. 2, 6, 14
- [38] A. Jahanian, X. Puig, Y. Tian, and P. Isola. Generative models as a data source for multiview representation learning. *arXiv preprint arXiv:2106.05258*, 2021. 2
- [39] J. Jian, X. Liu, M. Li, R. Hu, and J. Liu. Affordpose: A large-scale dataset of hand-object interactions with affordance-driven hand pose. In *ICCV*, 2023. 2
- [40] W. Jiang, N. Kolotouros, G. Pavlakos, X. Zhou, and K. Daniilidis. Coherent reconstruction of multiple humans from a single image. In *CVPR*, 2020. 5
- [41] Y. Jiang, S. Jiang, G. Sun, Z. Su, K. Guo, M. Wu, J. Yu, and L. Xu. Neuralhofusion: Neural volumetric rendering under human-object interactions. In *CVPR*, 2022. 2
- [42] T. Karras, S. Laine, and T. Aila. A style-based generator architecture for generative adversarial networks. In *CVPR*, 2019. 2
- [43] D. P. Kingma and J. Ba. Adam: A method for stochastic optimization. *arXiv preprint arXiv:1412.6980*, 2014. 13
- [44] A. Kirillov, Y. Wu, K. He, and R. Girshick. Pointrend: Image segmentation as rendering. In *CVPR*, 2020. 4, 7
- [45] A. Kirillov, E. Mintun, N. Ravi, H. Mao, C. Rolland, L. Gustafson, T. Xiao, S. Whitehead, A. C. Berg, W.-Y. Lo, P. Dollar, and R. Girshick. Segment anything. In *ICCV*, 2023. 7, 15
- [46] S. Kulal, T. Brooks, A. Aiken, J. Wu, J. Yang, J. Lu, A. A. Efros, and K. K. Singh. Putting people in their place: Affordance-aware human insertion into scenes. In *CVPR*, 2023. 2, 3
- [47] Y. J. Lee and K. Grauman. Predicting important objects for egocentric video summarization. *IJCV*, 2015. URL <https://api.semanticscholar.org/CorpusID:5617021>. 2
- [48] S. Levine and D. Shah. Learning robotic navigation from experience: principles, methods and recent results. *Philosophical Transactions of the Royal Society B: Biological Sciences*, 2022. 2
- [49] G. Li, V. Jampani, D. Sun, and L. Sevilla-Lara. Locate: Localize and transfer object parts for weakly supervised affordance grounding. In *CVPR*, 2023. 2
- [50] Z. Li, J. Sedlar, J. Carpentier, I. Laptev, N. Mansard, and J. Sivic. Estimating 3d motion and forces of person-object interactions from monocular video. In *CVPR*, 2019. 2
- [51] C.-H. Lin, J. Gao, L. Tang, T. Takikawa, X. Zeng, X. Huang, K. Kreis, S. Fidler, M.-Y. Liu, and T.-Y. Lin. Magic3d: High-resolution text-to-3d content creation. In *CVPR*, 2023. 3
- [52] S. Liu, Z. Zeng, T. Ren, F. Li, H. Zhang, J. Yang, C. Li, J. Yang, H. Su, J. Zhu, et al. Grounding dino: Marrying dino with grounded pre-training for open-set object detection. *arXiv preprint arXiv:2303.05499*, 2023. 7, 15
- [53] M. Loper, N. Mahmood, J. Romero, G. Pons-Moll, and M. J. Black. SMPL: A skinned multi-person linear model. *Proc. ACM SIGGRAPH Asia*, 2015. 7
- [54] A. Lugmayr, M. Danelljan, A. Romero, F. Yu, R. Timofte, and L. Van Gool. Repaint: Inpainting using denoising diffusion probabilistic models. In *CVPR*, 2022. 3
- [55] K.-K. Maninis, S. Popov, M. Nießner, and V. Ferrari. Cad-estate: Large-scale cad model annotation in rgb videos. In *ICCV*, 2023. 14
- [56] C. Mao, A. Cha, A. Gupta, H. Wang, J. Yang, and C. Vondrick. Generative interventions for causal learning. In *CVPR*, 2021. 2
- [57] M. McCool and E. Fiume. Hierarchical poisson disk sampling distributions. In *Graphics interface*, 1992. 5
- [58] L. Melas-Kyriazi, C. Rupprecht, I. Laina, and A. Vedaldi. Finding an unsupervised image segmenter in each of your deep generative models. *arXiv preprint arXiv:2105.08127*, 2021. 2
- [59] C. Meng, Y. He, Y. Song, J. Song, J. Wu, J.-Y. Zhu, and S. Ermon. SDEdit: Guided image synthesis and editing with stochastic differential equations. In *ICLR*, 2022. 3
- [60] M. Mihajlovic, S. Saito, A. Bansal, M. Zollhoefer, and S. Tang. COAP: Compositional articulated occupancy of people. In *CVPR*, 2022. 5, 13
- [61] R. Mokady, A. Hertz, K. Aberman, Y. Pritch, and D. Cohen-Or. Null-text inversion for editing real images using guided diffusion models. *arXiv preprint arXiv:2211.09794*, 2022. 3
- [62] A. Monszpart, P. Guerrero, D. Ceylan, E. Yumer, and N. J. Mitra. imapper: interaction-guided scene mapping from monocular videos. *ACM TOG*, 2019. 2
- [63] G. Moon, H. Choi, and K. M. Lee. Accurate 3d hand pose estimation for whole-body 3d human mesh estimation. In *CVPRW*, 2022. 3, 4, 13, 14
- [64] T. Nagarajan and K. Grauman. Learning affordance landscapes for interaction exploration in 3d environments. In *NeurIPS*, 2020. 2
- [65] H. Oleynikova, A. Millane, Z. Taylor, E. Galceran, J. Nieto, and R. Siegwart. Signed distance fields: A natural representation for both mapping and planning. In *RSS 2016 workshop*, 2016. 5, 13, 16
- [66] OpenAI. Chatgpt: Optimizing language models for dialogue. <https://openai.com/blog/chatgpt/>, 2023. 14
- [67] OpenAI. Gpt-4v(ision) system card. <https://openai.com/research/gpt-4v-system-card>, 2023. 3, 4, 12, 15
- [68] X. Pan, B. Dai, Z. Liu, C. C. Loy, and P. Luo. Do 2d gans know 3d shape? unsupervised 3d shape reconstruction from 2d image gans. *arXiv preprint arXiv:2011.00844*, 2020. 2
- [69] G. Pavlakos, V. Choutas, N. Ghorbani, T. Bolkart, A. A. Osman, D. Tzionas, and M. J. Black. Expressive body capture: 3d hands, face, and body from a single image. In *CVPR*, 2019. 3, 4, 7, 13
- [70] W. Peebles, J.-Y. Zhu, R. Zhang, A. Torralba, A. A. Efros, and E. Shechtman. Gan-supervised dense visual alignment. In *CVPR*, 2022. 2
- [71] I. A. Petrov, R. Marin, J. Chibane, and G. Pons-Moll. Object

- pop-up: Can we infer 3d objects and their poses from human interactions alone? In *CVPR*, 2023. 2, 16
- [72] B. Poole, A. Jain, J. T. Barron, and B. Mildenhall. Dreamfusion: Text-to-3d using 2d diffusion. In *ICLR*, 2023. 3
- [73] D. Rempe, L. J. Guibas, A. Hertzmann, B. Russell, R. Villegas, and J. Yang. Contact and human dynamics from monocular video. In *ECCV*, 2020. 2
- [74] E. Richardson, G. Metzer, Y. Alaluf, R. Giryes, and D. Cohen-Or. Texture: Text-guided texturing of 3d shapes. In *Proc. ACM SIGGRAPH*, 2023. 6, 14
- [75] R. Rombach, A. Blattmann, D. Lorenz, P. Esser, and B. Ommer. High-resolution image synthesis with latent diffusion models. In *CVPR*, 2022. 2, 3, 4, 12, 15
- [76] J. Romero, D. Tzionas, and M. J. Black. Embodied hands: Modeling and capturing hands and bodies together. *Proc. ACM SIGGRAPH Asia*, 2017. 7
- [77] M. Savva, A. X. Chang, P. Hanrahan, M. Fisher, and M. Nießner. Pigraphs: learning interaction snapshots from observations. *ACM TOG*, 2016. 2
- [78] SG_161222. Realistic vision v5.1. <https://civitai.com/models/4201?modelVersionId=130090>, 2023. 12, 15
- [79] C. E. Shannon. A mathematical theory of communication. *ACM SIGMOBILE*, 2001. 6
- [80] T. Shen, J. Gao, K. Yin, M.-Y. Liu, and S. Fidler. Deep marching tetrahedra: a hybrid representation for high-resolution 3d shape synthesis. In *NeurIPS*, 2021. 16
- [81] Sketchfab. Sketchfab. <https://sketchfab.com/>, 2023. 6
- [82] J. Sohl-Dickstein, E. Weiss, N. Maheswaranathan, and S. Ganguli. Deep unsupervised learning using nonequilibrium thermodynamics. In *ICML*, 2015. 2
- [83] J. Song, C. Meng, and S. Ermon. Denoising diffusion implicit models. *arXiv:2010.02502*, 2020. URL <https://arxiv.org/abs/2010.02502>. 2, 12
- [84] G. Sun, X. Chen, Y. Chen, A. Pang, P. Lin, Y. Jiang, L. Xu, J. Yu, and J. Wang. Neural free-viewpoint performance rendering under complex human-object interactions. In *ACM MM*, 2021. 2
- [85] M. J. Swain and D. H. Ballard. Color indexing. *IJCV*, 1991. 7
- [86] O. Taheri, N. Ghorbani, M. J. Black, and D. Tzionas. Grab: A dataset of whole-body human grasping of objects. In *ECCV*, 2020. 2
- [87] F. H. K. d. S. Tanaka and C. Aranha. Data augmentation using gans. *arXiv preprint arXiv:1904.09135*, 2019. 2
- [88] B. Trabucco, K. Doherty, M. Gurinas, and R. Salakhutdinov. Effective data augmentation with diffusion models. *arXiv preprint arXiv:2302.07944*, 2023. 2
- [89] S. Tripathi, A. Chatterjee, J.-C. Passy, H. Yi, D. Tzionas, and M. J. Black. DECO: Dense estimation of 3D human-scene contact in the wild. In *ICCV*, 2023. 1, 2
- [90] N. Tritrong, P. Rewatbowornwong, and S. Suwajanakorn. Repurposing gans for one-shot semantic part segmentation. In *CVPR*, 2021. 2
- [91] W. Wu, Y. Zhao, H. Chen, Y. Gu, R. Zhao, Y. He, H. Zhou, M. Z. Shou, and C. Shen. Datasetdm: Synthesizing data with perception annotations using diffusion models. *arXiv preprint arXiv:2308.06160*, 2023. 2
- [92] X. Xie, B. L. Bhatnagar, and G. Pons-Moll. Chore: Contact, human and object reconstruction from a single rgb image. In *ECCV*, 2022. 1
- [93] J. Xu, S. Zhu, H. Guo, and S. Wu. Automated labeling for robotic autonomous navigation through multi-sensory semi-supervised learning on big data. *IEEE TBD*, 2021. 2
- [94] S. Xu, Z. Li, Y.-X. Wang, and L.-Y. Gui. InterDiff: Generating 3d human-object interactions with physics-informed diffusion. In *ICCV*, 2023. 1, 2
- [95] L. Yang, X. Zhan, K. Li, W. Xu, J. Li, and C. Lu. CPF: Learning a contact potential field to model the hand-object interaction. In *ICCV*, 2021. 6
- [96] Y. Yang, W. Zhai, H. Luo, Y. Cao, J. Luo, and Z.-J. Zha. Grounding 3d object affordance from 2d interactions in images. In *ICCV*, 2023. 1, 2
- [97] Y. Ye, X. Li, A. Gupta, S. D. Mello, S. Birchfield, J. Song, S. Tulsiani, and S. Liu. Affordance diffusion: Synthesizing hand-object interactions. In *CVPR*, 2023. 2, 3
- [98] H. Yi, C.-H. P. Huang, D. Tzionas, M. Kocabas, M. Hassan, S. Tang, J. Thies, and M. J. Black. Human-aware object placement for visual environment reconstruction. In *CVPR*, 2022. 6
- [99] J. Y. Zhang, S. Pepose, H. Joo, D. Ramanan, J. Malik, and A. Kanazawa. Perceiving 3d human-object spatial arrangements from a single image in the wild. In *ECCV*, 2020. 14
- [100] S. Zhang, Y. Zhang, Q. Ma, M. J. Black, and S. Tang. Place: Proximity learning of articulation and contact in 3d environments. In *3DV*, 2020. 2
- [101] X. Zhang, B. L. Bhatnagar, S. Starke, V. Guzov, and G. Pons-Moll. Couch: Towards controllable human-chair interactions. In *ECCV*, 2022. 2
- [102] Y. Zhang, W. Chen, H. Ling, J. Gao, Y. Zhang, A. Torralba, and S. Fidler. Image gans meet differentiable rendering for inverse graphics and interpretable 3d neural rendering. *arXiv preprint arXiv:2010.09125*, 2020. 2
- [103] Y. Zhang, M. Hassan, H. Neumann, M. J. Black, and S. Tang. Generating 3d people in scenes without people. In *CVPR*, 2020. 2, 6
- [104] Y. Zhang, H. Ling, J. Gao, K. Yin, J.-F. Lafleche, A. Barriuso, A. Torralba, and S. Fidler. Datasetgan: Efficient labeled data factory with minimal human effort. In *CVPR*, 2021. 2
- [105] K. Zhou, B. L. Bhatnagar, J. E. Lenssen, and G. Pons-Moll. Toch: Spatio-temporal object correspondence to hand for motion refinement. In *ECCV*, 2022. 2
- [106] T. Zhou, R. Tucker, J. Flynn, G. Fyffe, and N. Snavely. Stereo magnification: Learning view synthesis using multi-plane images. In *Proc. ACM SIGGRAPH*, 2018. 14
- [107] C. Zimmermann, D. Ceylan, J. Yang, B. Russell, M. Argus, and T. Brox. Freihand: A dataset for markerless capture of hand pose and shape from single rgb images. *ICCV*, 2019. 1

A. Implementation Details

A.1. Affordance Image Generation

A.1.1 Rendering Object from Multi-Viewpoints

For *static* type objects, we install 8 weak perspective cameras with 45° azimuth intervals. For *dynamic* type objects, we install 4 weak perspective cameras with 90° azimuth intervals. The elevation is set constant within $[0^\circ, 30^\circ]$ range, where the values differ by category. For dynamic objects, we perturb the object with random rotations and translations. Specifically, we uniformly sample the rotation in the form of Euler angle, where yaw, pitch, and roll are uniformly sampled from a predefined range. Random translations are sampled in a similar way, where each component of 3D displacement is sampled from a predefined range. Note that we set weak perspective camera scale and distance from the object as hyperparameters. We repeat the rendering procedures 10 times with different perturbations applied, resulting in 40 distinct views.

A.1.2 Inpainting Mask Selection

We also render the inpainting masks while rendering the object, using the same camera parameters. Specifically, for each camera, we place an upright window perpendicular to the xy plane, also perpendicular to the xy projection of the camera’s front vector. For each mask, the center of the intersection with $z = 0$ plane lies within the xy projection of the 3D object. Note that the strides of the upright windows w.r.t. x, y direction are given as hyperparameters, along with the height and width of the window. We render these upright windows using assigned cameras to obtain 2D rectangular masks, consequently used as inpainting masks that occlude the original object. To reduce the number of unnecessary masks (e.g., masks that do not cover the object but mostly the background), we only retain the masks if the IoU (Intersection over Union) between the mask and the original object lies within the predefined range, also given as hyperparameters.

A.1.3 Prompt Generation

We generate human-object interaction prompts via GPT4v [67], where we input the rendered object image and the following query template:

Generate at most 3 simple subject-verb-object prompt where subject’s word is exactly ‘1 person’ and object’s image is given. You should use diverse and general word but no pronoun for subject. Generated prompt must align with common sense. Verb must be simple as possible, and should depict physical interaction between subject and object. Also,

Table 3. **Examples of Generated HOI Prompts.** Our method utilizes GPT4v [67] to generate plausible set of HOI prompts, given the object image and a query template. We provide example prompts for BEHAVE [2] objects below.

Object Category	Generated HOI Prompts
Backpack	1 person wears the backpack 1 person zips the backpack 1 person carries the backpack
Chairblack	1 person sits on the chair 1 person adjusts the chair 1 person lifts the chair
Keyboard	1 person types on the keyboard 1 person cleans the keyboard 1 person holds the keyboard
Suitcase	1 person packs the suitcase 1 person drags the suitcase 1 person opens the suitcase

only the interaction with given object is allowed, and no other objects should be introduced in the prompt.

We do not augment the prompt except “*full body*”, where we empirically find this augmentation useful when generating the whole human body instead of a zoom-in shot of body parts (e.g., hand). We provide examples of generated HOI prompts in Tab. 3.

A.1.4 Adaptive Mask Inpainting

While we use a publicly available inpainting diffusion model (RealisticVision [75, 78]), we note that our adaptive mask algorithm is applicable to any inpainting diffusion model. We sample images with 45~50 denoising steps using DDIM [83] scheduler, with a classifier-free guidance scale of 11.0. During Adaptive Mask Inpainting, we dilate the adaptive mask using 3×3 kernel k with n_t times repeat:

$$k = \begin{bmatrix} 1 & 1 & 1 \\ 1 & 1 & 1 \\ 1 & 1 & 1 \end{bmatrix}, \quad n_t = \begin{cases} 20 & 50 > t \geq 45 \\ 10 & 45 > t \geq 40 \\ 5 & 40 > t \geq 35 \\ 4 & 35 > t \geq 30 \\ 3 & 30 > t \geq 25 \\ 2 & 25 > t \geq 20 \\ 1 & 20 > t \geq 15 \\ 0 & 15 > t \geq 0 \end{cases} \quad (10)$$

We also employ “Provoke Schedule” (refer to Algorithm. 1) for faster generation speed. The provoke scheduler determines whether to skip the mask adaptation step ($t \in$

ProvokeSchedule) or not ($t \notin \text{ProvokeSchedule}$) during timestep t . Specifically, we use the following schedule:

$$\text{ProvokeSchedule} = \{t \mid (40 \geq t \geq 2 \text{ and } t \text{ is even}) \text{ or } t = 45\} \quad (11)$$

A.2. Lifting 2D Affordance to 3D

A.2.1 Number of Joints Used during Triangulation

We use Hand4Whole [63] to predict 3D humans from images ($\mathbf{F}_{\text{human}}$ in Sec. 3.3). The model returns 1 global rotation (for pelvis joint) and 54 human joint rotations following the SMPL-X [69] format; which consists of 21 body joints, 15 + 15 hand joints, 1 jaw joint, and 1 + 1 eye joints. During Virtual Triangulation (Sec. 3.3), we add 21 OpenPose [7] joints (“nose”, “right eye”, “left eye”, “right ear”, “left ear”, “left big toe”, “left small toe”, “left heel”, “right big toe”, “right small toe”, “right heel”, “left thumb”, “left index”, “left middle”, “left ring”, “left pinky”, “right thumb”, “right index”, “right middle”, “right ring”, “right pinky”) and exclude 11 original joints (“spine1”, “spine2”, “spine3”, “left foot”, “right foot”, “left collar”, “right collar”, “head”, “jaw”, “left eye smplhf”, “right eye smplhf”), resulting in $1 + 54 + 21 - 11 = 67$ joints.

A.2.2 Depth Initialization

We evenly space 7 human candidates along the orthographic rays, where we place the pelvis joint of 4th candidate (center candidate) to the position that minimizes the average distance w.r.t. the all object vertices. The distance between human candidates is proportional to the width of the human along the orthographic camera ray, where we set the multiplier as 0.3. We initialize the depth using the human candidate with maximum IoU between the rendered human mask and the predicted human segmentation mask.

A.2.3 Selecting Inliers for Multiview Human Cues

Given the human image (i.e., reference image) we aim to specify the depth, we first select the 2D joints from different view images (generated from the same prompt) to use for triangulation. Specifically, we first triangulate the 2D joints w.r.t. the corresponding joints in the reference image human, and filter the joints if the reprojection error is over 100. We iterate through the remaining joints again, where we triangulate the joint with other remaining joints and consequently apply RANSAC [18] to retain the inlier joints (we consider the joint as inlier if the reprojection error is less than 200). We finally select the maximum inlier set and use them as multiview cues for depth optimization.

A.2.4 Collision Loss

We implement collision loss using COAP [60], which represents the human body as SDF [65] field with a zero-level set of $f_{\Theta}(q|\mathcal{G}) = 0$, where \mathcal{G} is a human bone transformation and q is a query point. By treating query point q as an object vertex, we reduce collision between human and object by penalizing object vertices inside the human volume:

$$\mathcal{L}_{\text{collision}} = \frac{1}{N_o} \sum_{\mathbf{v}_i^o \in \mathbf{M}^o} \sigma(f_{\Theta}(\mathbf{v}_i^o|\mathcal{G})) \mathbf{1}(f_{\Theta}(\mathbf{v}_i^o|\mathcal{G}) > 0) \quad (12)$$

where $\sigma(\cdot)$ is the sigmoid function to convert SDF values to opacity and $\mathbf{1}(\cdot)$ returns 1 if the argument inside is true else 0. We set $\lambda_{\text{collision}} = 400$, and use Adam [43] optimizer with learning rate 1×10^{-2} for 200 iteration to optimize \mathcal{L} .

A.2.5 Filtering

We filter out the 3D human samples if (1) the IoU between the human rendering and predicted human segmentation is below 0.3 or over 0.8, (2) number of inliers after RANSAC [18] is below τ_{inlier} (which varies from 1 ~ 50, based on the given 3D object), or (3) the intersection volume over human volume is higher than 0.01.

A.3. Canonicalization for Primitive Extraction

We address 2 types of 3D object (including 3D human): (1) the object is assumed rigid, meaning that current object can be obtained via applying rigid transformation $\mathbf{T}^{\text{original} \rightarrow \text{current}} \in \text{SE}(3)$ on the original object; or (2) the object is non-rigid (e.g., 3D human), meaning that no original object exist, and also the rigid transformation. We provide the canonicalization procedure that addresses both cases.

Given the human surface normal \mathbf{n}_j^h and relative position $\mathbf{p}^{o \rightarrow h}$, we rotate them the same amount when rotating the object surface normal \mathbf{n}_i^o to face $\hat{\mathbf{n}} = [0, 0, 1]^T$ (or conversely, rotate object surface normal \mathbf{n}_i^o and relative position $\mathbf{p}^{h \rightarrow o}$ the same amount when rotating human surface normal \mathbf{n}_j^h to face $\hat{\mathbf{n}} = [0, 0, 1]^T$, which we omit for brevity). Specifically, we canonicalize the human normal \mathbf{n}_j^h to $\hat{\mathbf{n}}$ following:

$$\mathbf{n} = (\mathbf{n}_i^o \cdot \hat{\mathbf{n}}) \mathbf{n}_j^h + (\mathbf{n}_j^h \cdot \mathbf{n}_i^o) \hat{\mathbf{n}} - (\mathbf{n}_j^h \cdot \hat{\mathbf{n}}) \mathbf{n}_i^o + \left[\frac{\mathbf{n}_j^h \cdot (\mathbf{n}_i^o \times \hat{\mathbf{n}})}{1 + \mathbf{n}_i^o \cdot \hat{\mathbf{n}}} \right] (\mathbf{n}_i^o \times \hat{\mathbf{n}}) \quad (13)$$

and similarly, we canonicalize the relative position $\mathbf{p}^{o \rightarrow h}$ to \mathbf{p} following:

$$\mathbf{p} = (\mathbf{n}_i^o \cdot \hat{\mathbf{n}}) \mathbf{p}^{o \rightarrow h} + (\mathbf{p}^{o \rightarrow h} \cdot \mathbf{n}_i^o) \hat{\mathbf{n}} - (\mathbf{p}^{o \rightarrow h} \cdot \hat{\mathbf{n}}) \mathbf{n}_i^o + \left[\frac{\mathbf{p}^{o \rightarrow h} \cdot (\mathbf{n}_i^o \times \hat{\mathbf{n}})}{1 + \mathbf{n}_i^o \cdot \hat{\mathbf{n}}} \right] (\mathbf{n}_i^o \times \hat{\mathbf{n}}) \quad (14)$$

The canonicalization procedure described in Eq. 13 and Eq. 14 preserves the length of the vector ($\|\mathbf{n}\| = \|\mathbf{n}_j^h\|$ & $\|\mathbf{p}^{o \rightarrow h}\| = \|\mathbf{p}\|$) and preserves the orientation w.r.t. the object normal ($\mathbf{n}_i^o \cdot \mathbf{n}_j^h = \hat{\mathbf{n}} \cdot \mathbf{n}$ & $\mathbf{n}_i^o \cdot \mathbf{p}^{o \rightarrow h} = \hat{\mathbf{n}} \cdot \mathbf{p}$). Also, the



Figure 11. **Application of Contact & Orientation Tendency.** Leveraging the contact and orientation tendency information derived from our method, we present a fully automatic CAD model fitting pipeline for the task of *3D Scene Reconstruction from Single Image*. The proposed pipeline is zero-shot (i.e., applicable for any CAD models in 3D scenes), and does not require any additional training.

procedure above describes the movement of human normal \mathbf{n}_j^h and relative position $\mathbf{p}^{o \rightarrow h}$ following the object normal, when the object normal is taking the “shortest path” to $\hat{\mathbf{n}}$ along the sphere surface \mathbb{S}^2 . Note that for the case of rigid object, we transform the current object (and corresponding human) back to the original state using $(\mathbf{T}^{\text{original} \rightarrow \text{current}})^{-1}$ before applying Eq. 13 and Eq. 14. For non-rigid objects (e.g., human mesh), we directly apply Eq. 13 and Eq. 14.

A.4. Texture Generation for InterCap [37]

InterCap [37] does not provide texture for the 3D objects, hence we generate the texture for the objects using an off-the-shelf mesh stylization method [74]. The text prompts used for stylization are generated using ChatGPT [66], where we insert the following query:

Give a simple appearance description of an object of given categories as a form of “a {category}, {appearance description}”.

B. Applications

Our method can generate 3D affordance samples (given as 3D human and object pairs), where we can learn the affordance primitives for versatile use. We provide example applications of the learned primitives below.

B.1. Application of Contact & Orientation tendency

We can learn the 3D affordance primitives for any CAD model using our method, and infer contact and orientation tendency information of the object; which opens up the possibility of leveraging human cues for CAD-related 3D tasks. We demonstrate this by addressing the task of *3D Scene Reconstruction from Single Image*. The idea is to generate human cues from the image, and utilize the human cues along with our contact and orientation tendency information to fit the 3D CAD models.

Given the image from CAD Estate [10, 55, 106], the pipeline starts by applying Adaptive Mask Inpainting

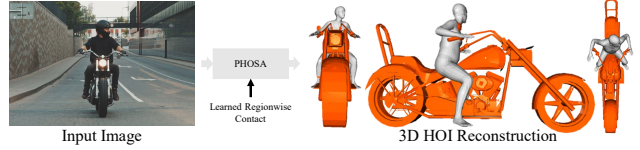


Figure 12. **Application of Regionwise Contact.** We can leverage the learned regionwise contact information derived from our method, to generalize and fully automate the existing pipeline [99] for the task of *3D Human-Object Reconstruction from Single Image*. The proposed pipeline is zero-shot (i.e., applicable for any 3D Object), and does not require any additional training.

(Sec. 3.2) to generate multiple images of humans interacting with the scene. We then predict 3D humans (and weak perspective camera parameters) from the generated images using off-the-shelf human prediction model [63]. Using the perspective camera parameters provided by CAD Estate [10, 55, 106], we convert the 3D humans from the weak perspective camera into perspective camera framework by optimizing human joint reprojection error, similar to CHORUS [26].

After placing the humans in 3D space, we utilize the learned contact and orientation tendency information to fit CAD model into 3D scenes. Specifically, we declare two losses: (1) Chamfer Distance between contact regions of human and object to resolve the proximity ambiguity; (2) Orientation Alignment Loss, where we choose the human vertex with high orientation tendency (j^*), and set the normal orientation with highest marginal probability value $\mathcal{P}_{ij^*}(\mathbf{n})$ as target human normal: which is used to align the object normals \mathbf{n}_i^o in a way such that the generated human normal of j^* -th vertex match the target human normal (after canonicalization via \mathbf{n}_i^o). By optimizing the rotation and translation of the CAD model w.r.t. the weighted sum of two losses, we can fit the CAD models into the 3D scene.

We demonstrate the results in Fig. 11. Our method is fully automated and *zero-shot*, meaning it is applicable to any CAD model. Also, since we leverage generated 3D human cues, our scene reconstruction results are human-aware.

B.2. Application of Regionwise Contact

From our learned primitives, we can also infer regionwise contact (as described in Sec. 5.3) between humans and objects. We can directly apply this information to improve existing pipelines for the task of *3D Human-Object Reconstruction from Single Image*. Specifically, we can improve PHOSA [99], which requires manual annotation of regionwise contact as input. By simply replacing the manual provision of regionwise contact information with our automatically learned contact (easily derived from the primitives), we can fully automate the pipeline, only requiring a single image as input. Furthermore, we can make PHOSA *zero-shot*, as our method can potentially return regionwise contact information for *any* 3D objects, meaning that PHOSA can

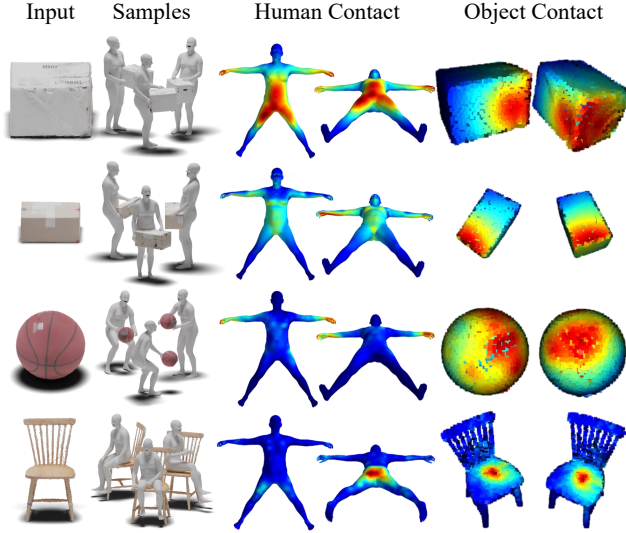


Figure 13. **Additional Results for Contactual Affordance.** We provide additional contactual affordance results for *boxlarge*, *boxmedium*, *basketball* and *chairwood* objects from BEHAVE [2].

also be applied to any 3D objects. We provide results in Fig. 12.

C. Additional Qualitative Results

We provide additional contactual affordance examples in Fig. 13, orientational affordance examples in Fig. 14, and spatial affordance examples in Fig. 15. Notably, the *monitor* example in Fig. 14 shows the strength of our method when modelling affordance even for objects without any physical interaction with the human. This is possible since the orientational affordance does not depend on proximity between object and human, as $f_{\text{orientation}}$ only depends on normal \mathbf{n} , thus marginalizing the effect of relative position \mathbf{p} when computing expectations as described in Sec. 4.

D. Limitations & Future Works

Spatial Bias in Inpainting Diffusion Models. Our method utilizes inpainting diffusion models [75, 78] to insert humans into object images; however, the diffusion model may possess spatial biases, which may alter the inpainting results as the properties of inpainting mask (e.g., center location, aspect ratio, resolution) differs. For example, diffusion model may not be able to generate humans if the objects that usually interact with hands (e.g., sports ball) are rendered on the bottom side of the image. Future research can further improve the spatial bias in diffusion models, or the mask selection procedure to reduce the number of unnecessary generations.

Incorrect HOI Prompt Generation. During the prompt generation step, there is a chance for the vision-language model [67] to misidentify the object in the image, resulting

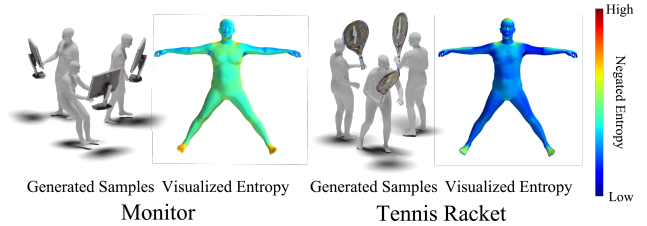


Figure 14. **Additional Results for Orientational Affordance.** We showcase the orientational affordance results for *monitor* and *tennis racket*.



Figure 15. **Additional Results for Spatial Affordance.** We showcase the spatial affordance results per body-part for *motorcycle*.

in incorrect HOI prompts that describe implausible situations for the given object.

Limits and Potentials of Adaptive Mask Inpainting. We propose an adaptive mask algorithm to preserve the original object during inpainting. However, the method depends on segmentation models to adapt the inpainting mask, and the errors during segmentation may affect the inpainting results. For example, if the segmentation model predicts part of the object as human due to various reasons (e.g., the texture of the object is similar to the texture of the generated human), the adaptive mask algorithm may not work well as the following inpainting mask occludes the object also. One potential approach for improvement is to use better segmentation models, such as Grounded SAM [45, 52]. Also, while we use adaptive mask inpainting only for the human insertion task, the algorithm can be applied to any categories the segmentation model allows, opening possibilities such as *open-vocabulary object insertion into scene image*.

Potentials of Virtual Triangulation. During virtual triangulation, we select the inlier joints from different views to optimize the depth of the 3D human. Since the inlier joint set exists for every 3D human, one promising future direction includes utilizing these inlier sets to cluster the multimodal distribution of affordance and find modes (e.g., a person may sit on the chair, but also stand on the chair).

Bias due to Filtering. Employing heavy filtering at the end of the pipeline may result in bias. For example, filtering out humans with high collision may cause the remaining samples to “slide out” the object, especially if the object is complex and is highly likely to collide given the plausible posture (e.g., motorcycle). One alternative is applying soft filtering (i.e., applying confidence weights instead of removing images with hard thresholds).

Low Granularity. Our primitive representation returns pointwise normal distribution, which consumes large memory when the resolution of human and object mesh is high;

enforcing the method to downsample the human and object mesh (refer to Sec. 4). Such limits in resolution may cause a lack of details, especially when modeling interactions with dexterous objects. It is worth exploring the use of implicit 3D representation for human and object surfaces (e.g., SDF [65], DMTet [80]), as such representations model the continuous surface as function.

Modelling Dexterous Interactions. Besides the limits due to low granularity, the limits in the diffusion model and 3D human prediction model also hinder modeling dexterous interactions (e.g., cup). For example, the diffusion model may struggle to generate high-quality hands when generating humans. For future research, employing diffusion models specifically trained on hand images to generate hand images, and using close-view (toward hand) cameras could be beneficial.

Possible Improvements in Primitives and its Derivatives.

We present a novel primitive representation of 3D affordance, and provide a way to derive contact information. While the method to derive contact is justified, there is room for improvement from the current definition of f_{contact} : for example, one may consider modeling pressure, to further generalize our representation to deformable objects. The orientational affordance term also has room for improvement. While the current definition of orientational affordance quantifies the tendency of orientation effectively (as a negated entropy term), it does not regard the main source of the tendency. For example, in the example of chair, the feet also pose a high tendency as feet usually head toward the ground; however, it is unfounded to say that the object causes such tendency; it is more likely to say it is due to gravitational pull. A promising future direction is to distinguish and quantify the source of orientational tendency.

Expanding to Non-Watertight Mesh. Our primitive representation can be easily extracted from non-rigid mesh (e.g., human mesh), as long as the mesh provides a closed surface and surface normal can be defined. One possible future direction is to improve the primitive representation to be easily extractable from any 3D surfaces (mesh or other surface representations), including non-watertight mesh, and sharp meshes where defining surface normals is non-trivial.

Evaluation Metrics. As the first in this direction, we evaluate and justify our method with simple metrics proposed in Sec. 5.2. It is worth exploring additional metrics to effectively quantify the validity of our method, especially for comparing the volumetric quality of 3D humans and objects for justification of 2D-to-3D lifting methods.

Potential Applications. Our new method and representation provide multitudes of possible applications, as demonstrated in Sec. B. We list potential downstream applications: (1) Large-scale 3D affordance dataset generation; (2) Object recognition from 3D human posture (similar to Object Pop-up [71]); (3) Action recognition from human-object interac-

tion sequence; (4) Application for robotics, especially for humanoids.